PHYSICAL REVIEW B VOLUME 31, NUMBER 8 15 APRIL 1985

Theoretical investigation of the optical spectra of LiC_6

Nan-Xian Chen and Sohrab Rabii
Moore School of Electrical Engineering, and Laboratory for Research on the Structure of Matter,
University of Pennsylvania, Philadelphia, Pennsylvania 19104

(Received 13 November 1984)

The complex dielectric tensor of LiC_6 has been calculated within the relaxation-time approximation based on the *ab initio* self-consistent-field energy band structure of this compound. The results are used to obtain reflectivity and electron-energy-loss spectra for both polarizations, parallel and perpendicular to the **c** axis. The results are in excellent agreement with various experimental measurements (see preceding paper) and serve both as a check on the accuracy of the calculated band structure and also as a clarification for the origin of the observed plasmons in LiC_6. Some of the conclusions appear to be applicable to other alkali-metal graphite intercalation compounds.

I. INTRODUCTION

LiC_6 is the alkali-metal graphite intercalation compound with the largest concentration of the intercalant. LiC_6 is often considered as a prototype for stage-1 alkali-metal graphite intercalation compounds, even though its structure, $A\alpha A\alpha\ldots$, is different from the others, which have the chemical composition MC_8 and the layer stackings of either $A\alpha A\beta A\gamma A\delta\ldots$ or $A\alpha A\beta A\gamma\ldots$.

In recent years there has been a great deal of interest in measurements directed at obtaining the optical spectra of this compound.[1–5] Furthermore, several theoretical investigations of the electronic structure of LiC_6 have been carried out.[6–10] In this paper we report on our *ab initio* calculation of $\tilde{\epsilon}(\omega)$, the complex dielectric tensor of LiC_6, similar in approach to our previous study of graphite.[11] Some preliminary results of this work have already been presented elsewhere.[12] In Sec. II we present a brief outline of the formalism for the dielectric tensor. In Sec. III the energy-band calculation on which this work is based is discussed with the details of the computational procedure given in Sec. IV. The relevant experimental results are reviewed in Sec. V. Our calculated results and their comparison with experiment[3,4] are given in Sec. VI, with the conclusion and discussion in Sec. VII.

II. FORMALISM

The calculation is carried out within the relaxation-time approximation. The contributions to the dielectric tensor are divided into two parts, the interband and intraband components. The former is given by[13]

$$\Delta\epsilon_{\alpha\beta}^{\text{inter}} = \frac{-4\pi e^2\hbar}{\omega} \sum_{c,v}{}' \int d\mathbf{k} \frac{\langle c\,|\,v_\alpha\,|\,v\rangle\langle v\,|\,v_\beta\,|\,c\rangle}{E_{cv}} \times \left[\frac{1}{E_{cv}-\hbar\tilde{\omega}} - \frac{1}{E_{cv}+\hbar\tilde{\omega}}\right], \quad (1)$$

where $\tilde{\omega}=\omega+i/\tau$, with τ the phenomenological scattering time, and $E_{cv}(\mathbf{k})=E_c(\mathbf{k})-E_v(\mathbf{k})$, with the primed summation taken over states such that $E_c > E_F > E_v$, where E_F is the Fermi energy. E_c, E_F, and E_v are obtained from a self-consistent-field (SCF) band-structure calculation using norm-conserving pseudopotentials.[10]

The intraband contribution to $\tilde{\epsilon}(\omega)$ is obtained from a Drude model as

$$\Delta\epsilon_{\alpha\beta}^{\text{intra}} = \sum_i \frac{-(\omega_{pi})^2\delta_{\alpha\beta}}{\omega(\omega+\hbar/\tau_i')}, \quad (2)$$

where i is over all the bands crossing the Fermi level, and τ_i' is the relaxation time for ith band. $(\omega_{pi})_\perp$ and $(\omega_{pi})_{||}$ are taken from a theoretical analysis of the Fermi surface for LiC_6.[6]

III. COMPUTATIONAL PROCEDURES

A. Energy band structure and oscillator strength

The SCF energy band structure used as the basis for this calculation is an extension of the studies Holzwarth *et al.*[10] The technique used was the *ab initio* norm-conserving pseudopotential theory with the wave functions expanded in a mixed basis of plane waves and localized orbitals.[10] We have extended the previous calculation to cover a range of 45 eV in order to obtain the interband spectra over a large frequency range. The energy bands were calculated at a mesh of 30 points in $\frac{1}{24}$th of the Brillouin zone (Fig. 1). Figure 2 shows the resulting energy band structure along the high-symmetry directions. It also indicates the important transitions near these axes.

The nonlocal nature of the pseudopotential leads to additional terms in the oscillator strength beyond the momentum matrix element between the initial and final states $|\,i,\mathbf{k}\rangle$ and $|\,j,\mathbf{k}\rangle$. We estimate that the neglect of these terms leads to an error of less than 12% for oscillator strength (see Appendix). Thus the velocity matrix element is taken as

$$\langle i,\mathbf{k}\,|\,\mathbf{v}\,|\,j,\mathbf{k}\rangle = \frac{\hbar}{m}\sum_n [a_n^i(\mathbf{k})]^* a_n^j(\mathbf{k})(\mathbf{G}_n+\mathbf{k}). \quad (3)$$

$\mathbf{G}_n$ is a reciprocal-lattice vector and $a_n(\mathbf{k})$ is the coeffi-

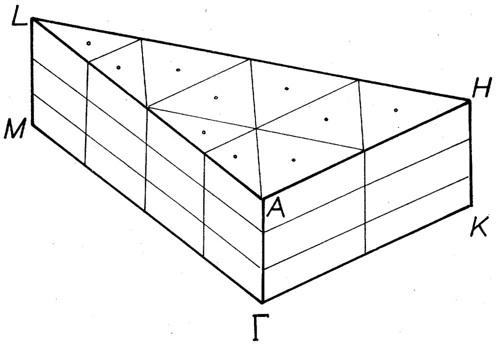

FIG. 1. Irreducible sector of the Brillouin zone of LiC$_6$ showing the mesh used as a basis for Gilat-Raubenheimer (GR) interpolation and **k**-space integration.

cient of the corresponding term in the plane-wave representation of these states, i.e.,

$$| i,\mathbf{k}\rangle = \sum_n a_n^j(\mathbf{k}) e^{i(\mathbf{G}_n+\mathbf{k})\cdot\gamma} . \tag{4}$$

In order to use this form, the localized-orbital parts of the final-state wave function were also expanded in ~ 1000 plane waves.

The increased number of bands due to the zone folding along with the choice of a finer mesh lead to a total number of calculated matrix elements that was 3 times that needed for graphite.

B. Interband contribution

Evaluation of Eq. (1) requires a summation over the Brillouin zone. This is achieved using a modification of the Gilat-Raubenheimer technique.[11,14] In this approach, the irreducible sector of the Brillouin zone ($\frac{1}{24}$th of the full zone in our case) is divided into a number of subcells, each containing one **k** point at which the *ab initio* energy bands and momentum matrix elements are calculated. Within each subcell the energy bands are expanded in a Taylor series, retaining only the first-order term (corresponding to a planar, constant-energy surface). In the modified approach, each subcell is replaced by a sphere having the same volume. The momentum matrix element is chosen to be constant within the subcell. The choice of the specific **k** points in the mesh was made in such a way that the original shape of the subcells would be as close to a sphere as possible. There are two advantages to this approximation. First, the shape of the subcell is independent of the Brillouin-zone geometry, and, second, the cross sections of the constant-energy surfaces within each subcell will have a circular shape, resulting in a considerably simplified computational procedure.

The choice of the scattering time τ is not very clearcut, especially since there is no experimental data for this parameter. Even though τ is, in general, both energy and momentum dependent, it is common practice to choose a single value for the relaxation time. If τ is chosen too large, the calculated spectra would contain many spurious structures which are produced by the finite integration mesh in the Brillouin zone. On the other hand, if the choice is too small, while we obtain smooth spectra, we may lose some real structure due to the unphysical broadening. Following the choice of 0.1×10^{-14} s for graphite,[11] we calculated the interband contribution to the spectra using three different values of τ, 0.2×10^{-14}, 0.5×10^{-14}, and 2.0×10^{-14} s. Since the integration mesh was finer for LiC$_6$ than for graphite,[11] we were able to use a somewhat larger value of τ, 0.2×10^{-14} s, for LiC$_6$, in the final calculation, and still obtain reasonably smooth spectra and good agreement with experimental data.

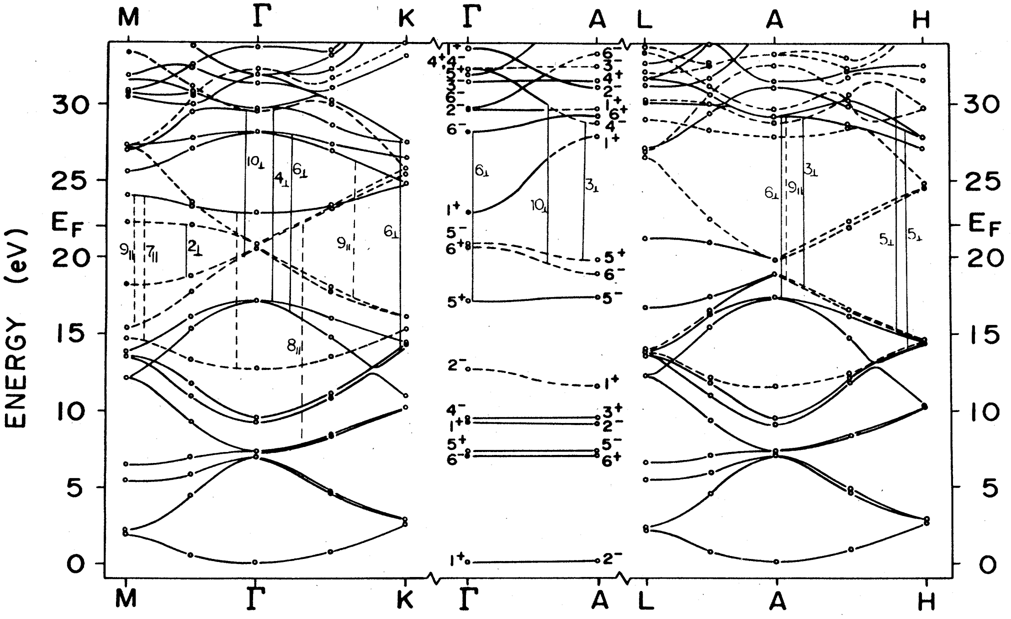

FIG. 2. Partial energy-band structure of LiC$_6$ along the high-symmetry axis. The arrows indicate some of the major optical transitions between these bands.

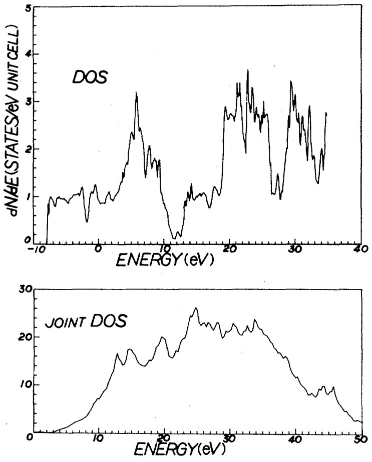

FIG. 3. The calculated density of states (DOS) and joint DOS for LiC_6.

The Fermi energy E_F is also required for evaluating the interband contribution. To obtain E_F, the density of states (DOS) is obtained by summing the contributions from each band i, within a subcell at k_0, as

$$\left[\frac{\partial n}{\partial E}\right]_{k_0,i} = \frac{2mS_{0i}}{(2\pi)^3 p_{0i}} , \tag{5}$$

where S_{0i} is the area of constant-energy surface in subcell $\mathbf{k}_0$ for band i, and p_{0i} is the magnitude of the diagonal component of the momentum matrix element for band i at point $\mathbf{k}_0$. Figure 3 shows our calculated DOS and joint DOS for LiC_6. By integrating the DOS we obtained the Fermi level for LiC_6 located ~ 1.4 eV above the π^* conduction bands at Γ. This is in good agreement with the results of various existing calculations presented in Table I, as well as with that estimated from joint DOS.

C. Intraband contribution

There are two conduction π^* bands that intersect the Fermi level in LiC_6. These are referred to as the upper (u) and lower (l) bands corresponding to their position in energy along the K—Γ—M or H—A—L directions in the Brillouin zone. Thus the Fermi surface is made of two pockets corresponding to these bands, similarly referred to as upper (u) and lower (l) surfaces, respectively.

The scattering time for carriers in both pockets is assumed to be the same, and is taken as 0.5×10^{-13} s, the same as for the graphite calculation.[11] Thus the summation over the carrier types in Eq. (2) can be replaced by an effective plasma frequency given as $\omega_p = (\omega_{pl}^2 + \omega_{pu}^2)^{1/2}$. Since both pseudopotential[10] and the Korringa-Kohn-Rostoker[6] (KKR) energy-band calculations gave nearly the same results in the vicinity of the Fermi energy, and since the ω_p for both types of carriers were already calculated in the latter work, these values were used in the present study (Table II).

TABLE I. Fermi energy in eV, measured from the bottom of π^* bands at Γ, and density of states at Fermi level in number of states per carbon atom per eV.

	Holzwarth[a]	Samuelson[b]	Volpilhac[c]	Present	Expt.[d]
E_F	1.4	1.4	1.8	1.4	
$N(E_F)$	0.24	0.25	0.22	0.18	0.21

[a] Reference 6.
[b] Reference 9.
[c] Reference 7.
[d] Reference 20.

TABLE II. Plasma frequencies in eV, for different carriers and different polarizations (Ref. 6).

Polarization	Upper band ω_{pu}	Lower band ω_{pl}	Effective ω_p
$\mathcal{E}\perp c$	5.2	4.1	6.7
$\mathcal{E}\parallel c$	1.9	0.9	2.2

IV. REVIEW OF THE EXPERIMENTAL RESULTS FOR LiC_6

Zanini, Basu, and Fischer,[1] and Basu *et al.*[2] performed the first reflectivity measurement on LiC_6 in the range below 3 eV for the polarization $\mathcal{E}\perp c$. Pfluger *et al.*[5] reported the reflectivity data up to 6 eV. Fischer *et al.*[3] have extended this measurement up to 11 eV with $\mathcal{E}\perp c$. They have also reported the reflectivity measurement with $\mathcal{E}\parallel c$ and energy below 3 eV. The latter measurement is not expected to be very accurate due to the difficulty of performing the experiment. The electron-energy-loss spectra (EELS) have been recently reported by Grunes *et al.*[4] from 0.3 to 288 eV, and ϵ_1 and ϵ_2 up to 40 eV were obtained from these results by Kramers-Kronig analysis. Since EELS involve transitions with finite q, the resulting dielectric function is expected to be different from $\epsilon(\omega,0)$, particularly at low energy. Therefore, Fischer *et al.*[3] combined the low-energy reflectivity with high-energy EELS data to perform the Kramers-Kronig analysis for the optical spectra of LiC_6.

V. COMPARISON OF THEORY AND EXPERIMENT

A. Imaginary part of dielectric function, $\epsilon_{2\perp}$

Figure 4 shows the comparison of the calculated result and those deduced from experiments.[3,4] It is seen that the overall agreement between theory and experiment is excellent. The major peaks for ϵ_2 at 4.0 and 13 eV are similar to those measured and calculated for pristine graphite.[11,15] The 4-eV peak comes mainly from π-π^* transitions "2" near the M point. This structure also exists for graphite, but due to the up-shift of the Fermi level, part ($\sim 50\%$) of the π^*-like final bands in graphite fall below the Fermi level in LiC_6 and lead to a reduction of the peak height. The agreement between calculated results and experiment is better than for graphite due to the use of a finer mesh in the calculation. The calculated results are in better agreement with the measured data obtained from reflectivity than for EELS. This can be attributed to the fact that the calculation and the reflectivity measurement both

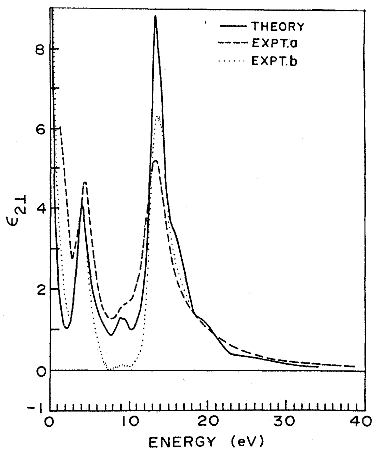

FIG. 4. $\epsilon_{2\perp}$ as a function of frequency for the polarization perpendicular to the c axis ($\mathscr{E}\perp\mathbf{c}$). The experimental results a and b are from Refs. 4 and 3, respectively.

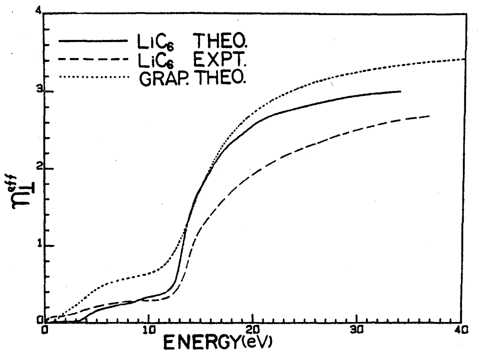

FIG. 5. Effective number of electrons for LiC$_6$ with $\mathscr{E}\perp\mathbf{c}$ as a function of frequency. The experimental result is from Ref. 3. The result for graphite is shown by a dotted line.

correspond to the $q=0$ case. The 13-eV structure has contributions mostly from σ-σ^* transitions distributed in the $K-H$ and $\Gamma-A$ regions (Fig. 2). This structure corresponds to transitions that are also allowed in graphite; however, due to zone folding they correspond to contributions from different regions in the LiC$_6$ Brillouin zone.

According to our calculation, there is a structure near 9 eV including two peaks located at 8.8 and 9.4 eV. It is in good agreement with the direct reflectivity measurement,[3] which shows structures at 8.4 and 9.1 eV. The former is mainly derived from transitions "3" near A, while the latter is attributed to transitions "10" from the region near $\Gamma-A$. The calculated strength for this structure is between the two experimental results,[3,4] i.e., it is smaller than the EELS but larger than the reflectivity data. This difference may be due to the fact that the EELS measurement is at finite q, thus overestimating the strength. Furthermore, the coarse mesh for momentum matrix elements in $\mathbf{k}$ space used in the calculation may lead to some inaccuracy in the result. These structures are absent in graphite but become allowed in LiC$_6$. From the band structure, we see that the up-shift of the Fermi level makes π-π^* transitions possible for π bands, which are above E_F in graphite and below E_F in LiC$_6$. Also, the backfolding of the $K-H$ bands of graphite into the $\Gamma-A$ region of the LiC$_6$ Brillouin zone, and unfolding along $\Gamma-A$, make the structure rather complicated.

Figure 5 shows the effective number of valence electrons per carbon atom in LiC$_6$ that have contributed to the photon absorption with $\mathscr{E}\perp\mathbf{c}$. The solid line is the calculated result and the dashed line is from experiment, while the dotted line represents the calculated result for graphite.[11] There are a total of $4\times6+1\times1=25$ valence electrons per unit cell of LiC$_6$. Since the $\sigma(1^+)$, the metal-graphite interlayer band, is completely above the Fermi level, the $2s$ electrons in Li atoms are completely transferred to the π^* bands of graphite. Thus from the point of view of the rigid-band model, each carbon has $\frac{25}{6}$ valence electrons.

Unlike graphite, the curve for LiC$_6$ starts at ~3 eV, which corresponds to an interband threshold in LiC$_6$ created by the raising of the Fermi level. The small absorption below this threshold is due to the intraband transitions. The inaccuracy of the calculations at very low frequency may be responsible for the difference between theory and experiment in this range. The height of the first plateau in LiC$_6$, ~0.3, is also reduced from that of graphite, ~0.6, due to the Fermi-level up-shift. This indicates that the π-π^* transitions in LiC$_6$ are reduced by $\sim50\%$ over that of graphite. In fact, the calculation of the density of states of LiC$_6$ also shows that the Fermi-level shift corresponds to a decrease of the effective number of electrons by ~0.3 for these transitions. The increased intraband plasma frequency of LiC$_6$, compared to graphite, leads to an overlap of the intraband the interband contributions to n_{eff}, and makes this plateau less flat than for graphite. There is also an indication that the two-dimensional nature of LiC$_6$ is weaker than for graphite, and thus the distinction of π- and σ-like bands does not hold in LiC$_6$ as well as it does in graphite. Taft and Phillip[15] have analyzed the optical data of graphite by separating the contributions of the π and σ bands. Fischer *et al.*[3] followed the same procedure in their analysis of the optical data for LiC$_6$, KC$_8$, RbC$_8$, and CsC$_8$. They found that this method works moderately well for KC$_8$, RbC$_8$, and CsC$_8$, but not for LiC$_6$. This is also indicated by the fact that the expansion of wave functions in LiC$_6$, especially for the states with high energies, include contributions from both p_z and sp_xp_y localized orbitals, corresponding to π and σ designations, respectively.

The final saturation value extending over 34 eV for in-plane polarization reaches $\sim76\%$, i.e., 18.3/25. This is better than expected for a totally *ab initio* calculation.[16] There is also an indication that the saturation would be reached at higher energy than in graphite.

B. Real part of the dielectric function, $\epsilon_{1\perp}$

The interpretation of ϵ_1 (Fig. 6) is somewhat more complicated. We have clearly identified two plasmons ω_{p1}^* and ω_{p3}^* at 2.85 and 25 eV, where the calculated ϵ_1 has zero crossings with positive derivatives. The sharp minimum at ~5 eV can be identified as a plasmon ω_{p2}^* even though no zero crossing occurs. In order to clarify

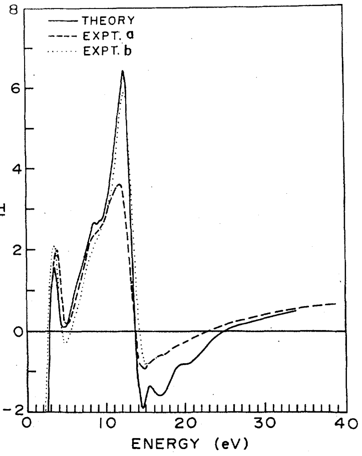

FIG. 6. $\epsilon_{1\perp}$ as a function of frequency for $\mathscr{E}\perp c$. The experimental results a and b are from Refs. 4 and 3, respectively.

the origin of these plasmons we recalculated ϵ_1 using an interband scattering time of 2×10^{-14} s, and we show the results along with the interband and intraband components in Fig. 7. The large scattering time used here results in the appearance of a zero crossing at 6.0 eV for the ω_{p2}^* plasmon and simplifies our present discussion. In Fig. 6, as in all the final calculations, the value of 0.2×10^{-14} s has been used for τ, as stated before.

First, we notice that the calculated plasmon ω_{p1}^*, even though clearly due to free carriers, occurs at much lower energy than the calculated, effective free-carrier plasma frequency, ω_{p1}, at 6.7 eV.[6] This is due to the screening of the free-carrier oscillations by the large positive component of interband contribution, $\Delta\epsilon_1^{\text{inter}}$, in this energy range. This situation is a general characteristic of the spectra of the alkali-metal graphite intercalation compounds, since in all cases the energy of the π-π^* transition occurs in the range in which the intraband effects are significant. For example, in KC_8 the intraband plasmon is observed at 2.38 eV and corresponds to the unscreened effective plasma frequency of 4.5 eV.[17] A related phenomenon has been observed in silver,[18] where the intraband oscillations of s electrons are screened by interband transitions involving the d electrons.

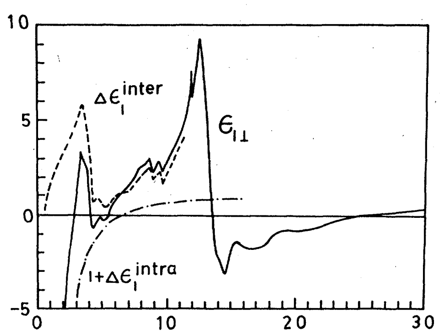

FIG. 7. Interband and intraband contributions to the real part of the calculated dielectric function.

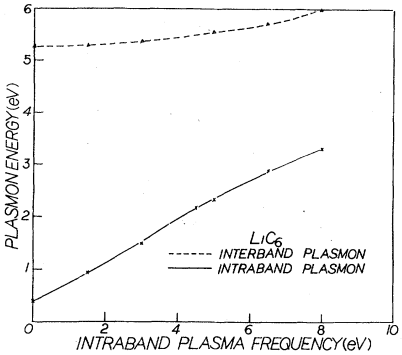

FIG. 8. Calculated positions for the free-carrier plasmon ω_{p1}^* and the first interband plasmon ω_{p2}^* as functions of the unscreened free-carrier plasma frequency ω_p.

The origin of the ω_{p2}^* plasmon is not immediately clear. Neither the interband nor the intraband contribution to the dielectric function separately go to zero at an energy in this range. However, if we plot the position of both ω_{p1}^* and ω_{p2}^* plasmons as a function of ω_{p1} (Fig. 8), we see that ω_{p1}^* varies strongly with ω_{p1}, while ω_{p2}^* does not. This not only confirms our previous identification of ω_{p1}^* as a free-carrier plasmon, but also leads us to label ω_{p2}^* as an interband plasmon, screened by free carriers. Figure 8 also indicates that, for $\omega_{p1}=0$, the value of ω_{p2}^* is 5.3 eV. This can then be taken as the energy of the unscreened interband plasmon ω_{p2}. The corresponding interband plasmon in graphite—which is essentially unscreened by free carriers—occurs at 6.3 eV. This plasmon, for both LiC_6 and graphite, is the first interband plasmon, and derives contributions from both π-π^* and σ-σ^* transitions. Taft *et al.* obtained a pure π-π^* plasma frequency of 11 eV for graphite by separating the π and σ contributions, which is different from the interband plasma frequency ω_{p2}. The calculated ω_{p2} is reasonably smaller than that for graphite due to loss of the π-π^* transition. Since the plasma frequency is proportional to the square root of the carrier density, the ratio of electrons involved in π-π^* transitions in LiC_6 to that of graphite should be $(5.3/6.3)^2$, which is $\sim70\%$. This is in rough agreement with the conclusion in Sec. V A. Figure 8 can also explain the position of intraband plasmon for $\mathscr{E}\parallel c$, since the screening effect is only dependent on charge distribution.

The plasmon ω_{p3}^*, occurring near 25 eV, is solely due to the interband transitions, since the free-carrier effects have disappeared at this energy. A similar plasmon is also observed in graphite. The structures near 15.5 and 19.5 eV in the ϵ_1 spectra which appear in both experimental and theoretical results stem from a number of σ-σ^* transitions, with significant oscillator strength distributed in almost all of the Brillouin zone. There are also two peaks at 15 and 19.5 eV in the joint density of states of LiC_6.

C. Electron-energy-loss and reflectivity spectra with $\mathscr{E}\perp c$

Figure 9 shows the calculated and measured[4] EELS, and again the agreement between theory and experiment is excellent. The plasmons observed in the calculated EELS correspond closely to those in the ϵ_1 spectra. This is an important check on the accuracy of the calculated results

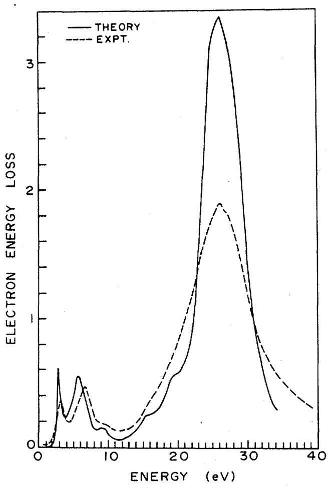

FIG. 9. Electron-energy-loss spectra for LiC$_6$. The experimental result is from Ref. 4.

imposed by the Kramers-Klonig relation between the imaginary and real parts of the conjugate pairs [such as Re$(1/\epsilon)$ and Im$(1/\epsilon)$]. There is, however, a 3-eV difference between the main peaks in the measured EELS and the zero crossing in the ϵ_1 spectra obtained from it by Kramers-Kronig analysis. This is the result of uncertainty in the extrapolation of the quantities that must be integrated in the process of carrying out this analysis. It is also due to the weak dependence of ϵ_1 and ϵ_2 on energy in the neighborhood of ω_{p3}. This dependence is critical in determining the position of the peak in the EELS.

Figure 10 shows our calculated reflectivity along with the experimental results of Fischer *et al.*[3] The latter is a combination of the direct measurement up to 11 eV plus the EELS measurement for the higher-energy range. As expected, the agreement between theory and experiment is much better in the lower-energy range, where the measurement of the reflectivity is direct and the band structure underlying the calculation is more accurate.

D. Spectra for $\mathscr{E}\parallel c$

In studying the calculated spectra for $\mathscr{E}\parallel c$, we are at a disadvantage, in that experimental results are available only for a very small energy range, i.e., below 3 eV.[3] For this reason we also compare our calculated results with those for graphite in order to better understand the spectra for LiC$_6$. Figures 11 and 12 show the calculated $\epsilon_{2\parallel}$ and $\epsilon_{1\parallel}$ for both materials. The free-carrier contribution clearly indicates the increased metallic behavior of LiC$_6$ compared to graphite. Furthermore, we observe more structure in the spectra for LiC$_6$ than for graphite. This could be the results of folding of the nearly parallel graphite bands into the small Brillouin zone of LiC$_6$ and the subsequent splitting of degeneracies due to intercalant carbon interactions.

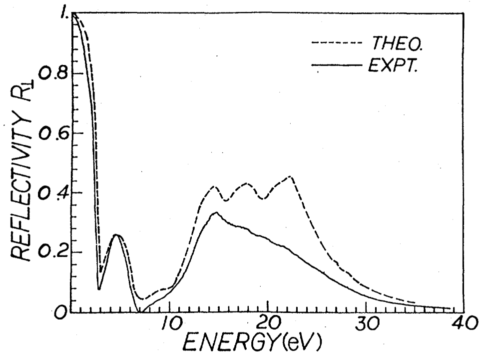

FIG. 10. Reflectivity with $\mathscr{E}\perp c$, $R_\perp(\omega)$. The experimental result is from Refs. 3 and 4.

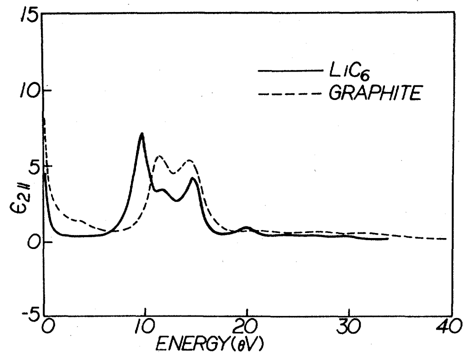

FIG. 11. Calculated imaginary part of the dielectric function, $\epsilon_{2\parallel}$, for LiC$_6$ and graphite.

The two large peaks in Fig. 11 for both graphite and LiC$_6$ have common origins. The first, near 10 eV, is due to the π- to the interlayer σ-band transitions in graphite and the π-to "metal" σ-band transitions in LiC$_6$. These transitions occur at a lower energy in LiC$_6$ than in graphite due to the fact that the separation of the "metal-interlayer" band from the graphite-like valence-band complex is smaller in LiC$_6$ than in graphite. The second peak is due to the σ-π^* transition and is at about the same energy in both materials. We see a small peak in LiC$_6$ spectra occurring between the previous two. This is due to π-σ^* transitions "9" around point A in the Brillouin zone (Fig. 2). Even though the same transition occurs in graphite near K (K in graphite folds to A in LiC$_6$), it is not seen in graphite spectra due to the overlap with the large first peak.

The structures near 20 eV in the calculated spectra are absent both in the calculated graphite spectra and the measured results for LiC$_6$. Since the calculation for LiC$_6$

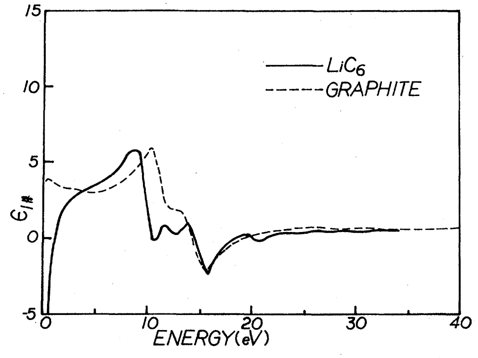

FIG. 12. Calculated $\epsilon_{1\parallel}$ for LiC$_6$ and graphite.

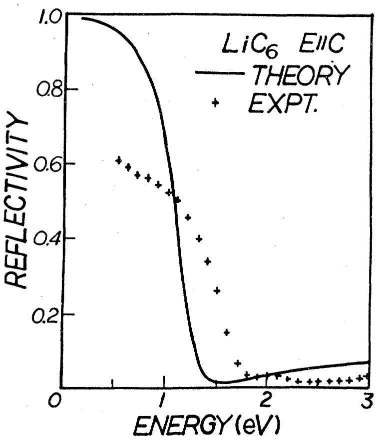

FIG. 13. Reflectivity with $\mathscr{E}\|\mathbf{c}$, $R_{\|}(\omega)$. The experimental result is from Ref. 3.

is expected to be more accurate than that for graphite, these structures may eventually be observed in an improved measurement.

Recently, Fischer *et al.*[3] reported carrying out a polarized reflectivity measurement, $R_{\|}(\omega)$, on a reasonably good "*a* face" (formed from the layer edges) of $\mathrm{LiC_6}$ from 0.5 to 3 eV. Even though this measurement is not expected to be very accurate due to the difficulty of preparing a satisfactory "*a* face," the comparison with theory (Fig. 13) shows that the overlap of the intraband and interband effects leads to a screening of the intraband plasmon. If we define the position of the plasmon as the middle point of the Drude edge, then we see a reasonable agreement between the positions of the calculated and measured plasmons which occur at 1.2 and 1.4 eV, respectively. This plasmon corresponds to a calculated unscreened plasma frequency $\omega_{p\,\|}$ of 2.2 eV (Table II).

VI. CONCLUSION AND DISCUSSION

The calculated dielectric function is in excellent agreement with experiment and successfully explains the origin of the observed plasmons. It also provides a good test for the quality of the calculated *ab initio* SCF energy band structure of this compound. The comparison of this calculation with that performed for graphite, using an identical approach, points to the generality of the formalism and the transferability of the norm-conserving pseudopotential for the same atom to different materials.

ACKNOWLEDGMENTS

We gratefully acknowledge helpful suggestions from N. A. W. Holzwarth, J. E. Fischer, R. C. Tatar, E. J. Mele, D. P. DiVincenzo, M. E. Preil, and C. C. Shieh, and the resources provided by the Moore School Computing Facility at the University of Pennsylvania. This work was supported by National Science Foundation Materials Research Laboratories Grant No. DMR-82-16718, and U.S. Army Research Office Contract No. DAAG-29-80-C400.

APPENDIX

The oscillator strength for the dipole transitions, in general, is expressed in terms of the matrix element of the velocity operator. If the potential is local, this will reduce to the matrix element of the momentum operator. We will give both quantum-mechanical and semiclassical prescriptions for obtaining the correction to the momentum matrix when the potential is nonlocal. In our calculation, the nonlocal potential for a crystal is expressed by

$$V_{nl}(\mathbf{r},\mathbf{r}')=\sum_{\mathbf{T},\tau}\frac{\delta(|\mathbf{r}-\tau-\mathbf{T}|-|\mathbf{r}-\tau-\mathbf{T}|)}{|\mathbf{r}-\tau-\mathbf{T}|^2}\times\sum_{L}\delta V_L(|\mathbf{r}-\tau-\mathbf{T}|)\times\sum_{M}Y^*_{LM}(\mathbf{r}-\tau-\mathbf{T})Y_{LM}(\mathbf{r}-\tau-\mathbf{T})\,, \tag{A1}$$

where $\mathbf{T}$ is a lattice-translation symmetry vector, τ is an atomic-site vector, and $\delta V_L(r)$ is the radial part of the lth component of the nonlocal potential.

1. Quantum-mechanical approach

The velocity operator is given by

$$\mathbf{v}=\dot{\mathbf{r}}=[\mathbf{r},H]/i\hbar=\mathbf{p}/m+[\mathbf{r},V_{nl}]/i\hbar\,. \tag{A2}$$

In a plane-wave representation, the nonlocal correction term becomes

$$\begin{aligned}\langle\mathbf{q}_2|[r_\mu,V_{ml}]|\mathbf{q}_1\rangle=&-16\pi^2Y_{1\mu}(\Omega_{\mathbf{q}_2})\sum_{l,m}i^{l+1}Y_{lm}(\Omega_{\mathbf{q}_1})\int dr\,r^3J_l(q_2r)J_1(q_1r)\delta V_l(r)\\&-16\pi(4\pi)^{-1/2}\sum_{L,M,l,m}i^LC^{l1L}_{m\mu M}Y_{LM}(\Omega_{\mathbf{q}})\int dr\,r^3J_L(q_1r)J_0(q_2r)\delta V_l(r)\,,\end{aligned} \tag{A3}$$

where

$$C^{l1L}_{m\mu M}=\int Y^*_{LM}(\Omega)Y_{lm}(\Omega)Y_{1\mu}(\Omega)d\Omega \tag{A4}$$

are the Clebsh-Gordan coefficients.

2. Semiclassical approach

In the coordinate space, the effect of the operator $\hat{V}$ on the state $|\psi\rangle$ is[19]

$$\langle\mathbf{r}|V|\psi\rangle=\int V(\mathbf{r},\mathbf{r}')\psi(\mathbf{r}')d\mathbf{r}'\,.$$

Using the Taylor's expansion for $\psi(\mathbf{r}')$, we have

$$\langle \mathbf{r}\,|\,V\,|\,\psi\rangle = \left[\int V(\mathbf{r},\mathbf{r}')e^{i(\mathbf{r}'-\mathbf{r})\cdot\mathbf{p}}d\mathbf{r}'\right]\psi(\mathbf{r}) \equiv V(\mathbf{r},\mathbf{p})\psi(\mathbf{r})\,. \tag{A5}$$

Considering the short-range property of the norm-conserving pseudopotential, the overlap between different atomic nonlocal potentials can be ignored. Therefore, Eq. (A1) becomes

$$V(\mathbf{r},\mathbf{r}') = \sum_{l,m} \delta V_l(r)\frac{\delta(r-r')}{r^2}Y_{lm}^{*}(\Omega')Y_{lm}(\Omega)\,. \tag{A6}$$

Up to the linear term in p, we have $e^{i\mathbf{r}\cdot\mathbf{p}} \sim 1+\mathbf{r}\cdot\mathbf{p}$ and $J_l(pr) \sim (pr)^l/\Gamma(l+1)$. Within this approximation, Eqs. (A5) and (A6) result in

$$V(\mathbf{r},\mathbf{p}) = \frac{i\mathbf{p}\cdot\mathbf{r}}{r^2}(\delta V_0 - \tfrac{3}{2}\delta V_1)\,. \tag{A7}$$

We consider that the scalar nonlocal potential can be replaced by a local vector potential,

$$\mathbf{A} = \frac{im\mathbf{r}}{r^2}(\delta V_0 - \tfrac{3}{2}\delta V_1)\,. \tag{A8}$$

Therefore the corresponding velocity correction becomes

$$\Delta\mathbf{v} = e\mathbf{A}/m = i(\mathbf{r}/r^2)(\delta V_0 - \tfrac{3}{2}\delta V_1)\,. \tag{A9}$$

If the shapes of the crystal wave functions near the atomic sites do not change greatly from those in the atomic case, we can estimate the correction to a typical momentum matrix element by using the scaled atomic wave function for C 2s, C 2p, and Li 2s levels. The results indicate that the corrections are of the order of 3% or less for graphite and 12% or less for $\mathrm{LiC_6}$.

---

[1] M. Zanini, S. Basu, and J. E. Fischer, Carbon **16**, 211 (1978).

[2] S. Basu, C. Zeller, P. J. Flanders, C. D. Fuerst, W. D. Johnson, and J. E. Fischer, Mater. Sci. Eng. **38**, 275 (1979).

[3] J. E. Fischer, J. M. Bloch, C. C. Shieh, M. E. Preil, and K. Jelley, preceding paper [Phys. Rev. B **31**, 4773 (1985)].

[4] L. A. Grunes, I. P. Gates, J. J. Ritsko, E. J. Mele, D. P. DiVincenzo, M. E. Preil, and J. E. Fischer, Phys. Rev. B **28**, 6681 (1983).

[5] P. Pfluger, E. Schüpfer, R. Lapka, and H. J. Güntherodt, in *Extended Abstracts of the 15th Biennial Conference on Carbon,* edited by W. C. Forsman (American Carbon Society, University Park, PA, 1981), p. 70.

[6] N. A. W. Holzwarth, S. Rabii, and L. A. Girifalco, Phys. Rev. B **18**, 5190 (1978).

[7] G. Volpilhac and J. Hoarau, J. Phys. C **13**, 2281 (1980).

[8] G. Volpilhac, L. Ducasse, F. Achard, and J. Hoarau, Phys. Rev. B **23**, 4236 (1981).

[9] L. Samuelson and I. P. Batra, J. Phys. C **13**, 5105 (1980).

[10] N. A. W. Holzwarth, S. Louie, and S. Rabii, Phys. Rev. B **28**, 1013 (1983).

[11] N. X. Chen, S. Rabii, and N. A. W. Holzwarth, Synth. Met. **6**, 197 (1983).

[12] N. X. Chen and S. Rabii, Phys. Rev. Lett. **52**, 2368 (1984).

[13] H. Ehrenreich and H. R. Phillip, Phys. Rev. **115**, 786 (1959).

[14] L. G. Johnson and G. Dresselhaus, Phys. Rev. **87**, 2275 (1974).

[15] E. A. Taft and H. R. Phillip, Phys. Rev. **138**, A197 (1965).

[16] F. Wooten, *Optical Properties of Solids* (Academic, New York, 1972).

[17] D. P. DiVincenzo and S. Rabii, Phys. Rev. B **25**, 4110 (1982).

[18] H. Ehrenreich and H. R. Phillip, Phys. Rev. **128**, 1622 (1962).

[19] A. Starace, Phys. Rev. B **3**, 1242 (1971).

[20] P. Delhaes, J. C. Rouillon, J. P. Manceau, D. Guerard, and A. Hérold, J. Phys. (Paris) Lett. **37**, L127 (1976).